Geophys. J. Int. (2007) **168,** 1–12 doi: 10.1111/j.1365-246X.2006.03138.x

A modified least-squares collocation method for the determination of crustal deformation: first results in the Swiss Alps

R. Egli,[1]* A. Geiger,[1] A. Wiget[2] and H.-G. Kahle[1]

[1] *Geodesy and Geodynamics Lab, Swiss Federal Institute of Technology, ETH Hönggerberg,* 8093 *Zürich, Switzerland. E-mail: eglix007@umn.edu*
[2] *Swiss Federal Office of Topography, Seftigenstrasse* 264, 3084 *Wabern, Switzerland*

Accepted 2006 July 11. Received 2006 July 8; in original form 2004 October 31

SUMMARY

The calculation of recent crustal movements and the associated crustal deformation rely on a suitable interpolation of geodetic measurements with repetition cycles of years or decades and modern GPS permanent networks. A common interpolation methods is the least-square collocation (LSC). LSC requires some *a priori* assumptions about the characteristics of the velocity field, that is, stocasticity in Moritz's definition of LSC. We present a novel approach, called adaptative LSC (ALSC) to the interpolation of non-stochastic fields, which encompass the traditional LSC and the block model as special cases. This modified collocation method is based on the empirical estimation of a anisotropic and inhomogeneous covariance function of the interpolated field. The method has been tested on synthetic data that simulate geodetic measurements over a triple plate junction and with real data from precise levelling measurements over the Swiss Alps. In both cases, ALSC gave better and more stable results, compared to LSC and other interpolation methods, such as smoothed splines.

Key words: Alps, least-squares collocation, levelling, recent crustal movements.

1 INTRODUCTION

Least-squares collocation (LSC) is a generalized estimation method that has been applied successfully to the interpolation of potential field anomalies (Kaula 1963; Moritz 1978), and to the solution of various problems in physical geodesy (Moritz 1970a,b, 1980). LSC can be generalized to arbitrary data as a purely analytical approximation method (Grafarend 1976). Recently, LSC has been used to estimate crustal deformation fields from GPS measurements (e.g. Cocard *et al.* 1999; Kahle *et al.* 1995, 1999, 2000).

LSC is based on the minimization of the mean squared error (MMSE). We refer to Table 1 for mathematical notations. The mean squared error with respect to a Q-norm is defined as:

$$\|\varepsilon\|^2 = \varepsilon^{\mathrm{T}}\,\mathbf{Q}\,\varepsilon, \tag{1}$$

where $\varepsilon = \hat{\mathbf{x}} - \mathbf{x}$ is the difference between a measured field $\mathbf{x}$ and its estimate $\hat{\mathbf{x}}$ at the measurement points, and $\mathbf{Q}$ is a positive definite matrix (i.e. $\mathbf{v}^{\mathrm{T}}\mathbf{Q}\mathbf{v} > 0$ for any non-zero vector $\mathbf{v}$). Two distinct approaches to the minimization of eq. (1) have been proposed by Moritz (1970a) and Krarup (1969). Moritz's approach assumes a stochastic field, allowing an empirical choice of $\mathbf{Q}$, whereas Krarup's approach does not make restrictive assumptions about the field. On the other hand, it does not provide any physical criterion to fix a suitable Q-norm for the error estimation. Sansò (1980) demonstrated that Krarup's and Moritz's approaches are equivalent under the assumption of rotational invariance of the MMSE. Following his results, a linear estimator of a general field $x(\mathbf{r})$ measured at N points $\mathbf{r}_1 \ldots \mathbf{r}_N$ is:

$$\hat{x}(\mathbf{r}) = \sum_{k=1}^{N} \lambda_k(\mathbf{r}, \mathbf{r}_k)\, x(\mathbf{r}_k), \tag{2}$$

and eq. (1) is satisfied under rotational invariance when:

$$\lambda_k(\mathbf{r}, \mathbf{r}_k) = \sum_{j=1}^{N} X(\mathbf{r}, \mathbf{r}_k) X^{-1}(\mathbf{r}_j, \mathbf{r}_k), \tag{3}$$

where X is the covariance function of $x(\mathbf{r})$. The classic LSC solution:

$$\hat{\mathbf{x}} = \mathbf{C}_{\hat{x}x}\mathbf{C}_{xx}^{-1}\mathbf{x}, \tag{4}$$

for the estimated field $\hat{\mathbf{x}}$ at M prediction points $\mathbf{p}_1 \ldots \mathbf{p}_M$ follows from eqs (2) and (3) with the covariance matrices $[\mathbf{C}_{xx}]_{kj} = X(\mathbf{r}_k, \mathbf{r}_j)$ and $[\mathbf{C}_{\hat{x}x}]_{ij} = X(\mathbf{p}_i, \mathbf{r}_j)$. A problem of eq. (4) is that the covariance functions is generally unknown. An estimate of the covariance matrices is obtained with Moritz's stochastic approach by dividing $\mathbf{x}$ into

(i) a long-range contribution $\mathbf{t}$, sometimes called trend function,
(ii) a short-range, stochastic contribution $\mathbf{s}$, also called signal and
(iii) an observational error $\mathbf{n}$ (Fig. 1).

*Now at: the Institute for Rock Magnetism, University of Minnesota, 291 Shepherd Laboratories, 100 Union St. SE, Minneapolis MN 55455-0128, USA.

Table 1. List of mathematical notations used in the text and their meaning.

Symbol	Meaning
$\mathbf{C}_{nn}$	(Auto)covariance matrix of $\mathbf{n}$
$[\mathbf{C}_{ss}]_{kj} = T(\mathbf{r}_k, \mathbf{r}_j)$	(Auto)covariance matrix of $\mathbf{s}$
$\mathbf{C}_{\hat{s}s}]_{kj} = T(\mathbf{p}_k, \mathbf{r}_j)$	Covariance matrix of $\mathbf{s}$, $\hat{\mathbf{s}}$
$[\mathbf{C}_{tt}]_{kj} = T(\mathbf{r}_k, \mathbf{r}_j)$	(Auto)covariance matrix of $\mathbf{t}$
$\mathbf{C}_{\hat{t}t}]_{kj} = T(\mathbf{r}_k, \mathbf{r}_j)$	Covariance matrix of $\mathbf{t}$, $\hat{\mathbf{t}}$
$S(\mathbf{p}, \mathbf{r}) = E[\hat{s}(\mathbf{p})s(\mathbf{r})]$	Covariance function of $s(\mathbf{r})$, $\hat{s}(\mathbf{r})$
$S(\mathbf{r}_A, \mathbf{r}_B) = E[s(\mathbf{r}_A)s(\mathbf{r}_B)]$	(Auto)covariance function of $s(\mathbf{r})$
$T(\mathbf{p}, \mathbf{r}) = E[\hat{t}(\mathbf{p})t(\mathbf{r})]$	covariance function of $t(\mathbf{r})$, $\hat{t}(\mathbf{r})$
$T(\mathbf{r}_A, \mathbf{r}_B) = E[t(\mathbf{r}_A)t(\mathbf{r}_B)]$	(Auto)covariance function of $t(\mathbf{r})$
$E(v)$	Expected value of v
$\mathbf{n} = [n_1, \ldots, n_N]$	Observational errors of $\mathbf{x}$
$\mathbf{p}$	An interpolation point
$\mathbf{r}$	A measurement point
$s(\mathbf{r})$	Short-range component of $x(\mathbf{r})$
$t(\mathbf{r})$	Long-range component of $x(\mathbf{r})$
v	A variable
$\hat{v}$	Estimate of v
$\mathbf{v}$	A vector
$\|\mathbf{v}\|$	Euclidian norm of $\mathbf{v}$
$\|\|\mathbf{v}\|\|$	A general norm of $\mathbf{v}$
$x(\mathbf{r})$	A scalar field
$\mathbf{x} = [x_1, \ldots, x_N]$	Measurements of $x(\mathbf{r})$ at $\mathbf{r}_1, \ldots, \mathbf{r}_N$
$\tilde{\mathbf{x}} = [\tilde{x}_1, \ldots, \tilde{x}_N]$	Exact values of $x(\mathbf{r})$ at $\mathbf{p}_1, \ldots, \mathbf{p}_M$
$\hat{\mathbf{x}} = [\hat{x}_1, \ldots, \hat{x}_M]$	Estimated values of $x(\mathbf{r})$ at $\mathbf{p}_1, \ldots, \mathbf{p}_M$

Under this assumption, and if $\mathbf{n}$ and $\mathbf{s}$ are uncorrelated, eq. (4) becomes:

$$\hat{\mathbf{x}} = \hat{\mathbf{t}} + \mathbf{C}_{\hat{s}s}(\mathbf{C}_{ss} + \mathbf{C}_{nn})^{-1}(\mathbf{x} - \hat{\mathbf{t}}). \tag{5}$$

The long-range term $\mathbf{t}$ is usually inferred from a physical law or empirically by fitting the data with a model function. If LSC is applied on sufficiently small regions, $t(\mathbf{r})$ can be approximated adequately by a polynomial. The choice of $\mathbf{t}$ determines the statistical properties of $\mathbf{s}$, and does not necessarily guarantee its stocasticity.

In the calculation of crustal deformation fields, $t(\mathbf{r})$ may be identified with regional tectonic movements, and $s(\mathbf{r})$ with local effects produced by small-scale deformations. The observational error $\mathbf{n}$ includes the measurement error $\delta\mathbf{x}$, as well as spurious non-tectonic movements $h(\mathbf{r})$ of the measurement points due to local disturbances (e.g. anthropogenic effects). The distinction between $t(\mathbf{r})$, $s(\mathbf{r})$ and $h(\mathbf{r})$ is somewhat arbitrary, since it is based on what is known about $t(\mathbf{r})$ and on the expected statistical properties of $s(\mathbf{r})$ and $h(\mathbf{r})$. In the analysis of recent crustal movements (RCM), $t(\mathbf{r})$ is related to known tectonic structures. An example is the so-called block model, where the Earth's crust is divided into units, (the plates), separated by faults (e.g. McKlusky *et al.* 2001; Chen *et al.* 2004). The crustal strain is concentrated along the plate boundaries. On the other hand, a strain field over a homogeneous region (e.g. $\mathbf{t} = 0$) has been assumed successfully in many studies (McKenzie & Jackson 1986). In regions with a intermediate-scale, complex tectonic behaviour, such as the Alps, it is difficult to find an adequate model for $t(\mathbf{r})$.

In this paper we assume that $t(\mathbf{r})$ is a fully unknown field. In order to deal with the superposition of a long- and a short-range term, a new LSC interpolation method is presented, which does not require a predefined model for $t(\mathbf{r})$.

2 INHOMOGENEOUS, ANISOTROPIC LEAST-SQUARES COLLOCATION

The general form of a LSC solution is given by eq. (4), whereby the covariance matrices are unknown. The covariance function of a non-stochastic field in its most general form is inhomogeneous (e.g. Rummel & Schwarz 1977) and anisotropic (e.g. Morrison 1977). Hence, the covariance function $T(\mathbf{r}_A, \mathbf{r}_B)$ of $t(\mathbf{r})$ is inhomogeneous and anisotropic, since the covariance function $S(r_{AB})$

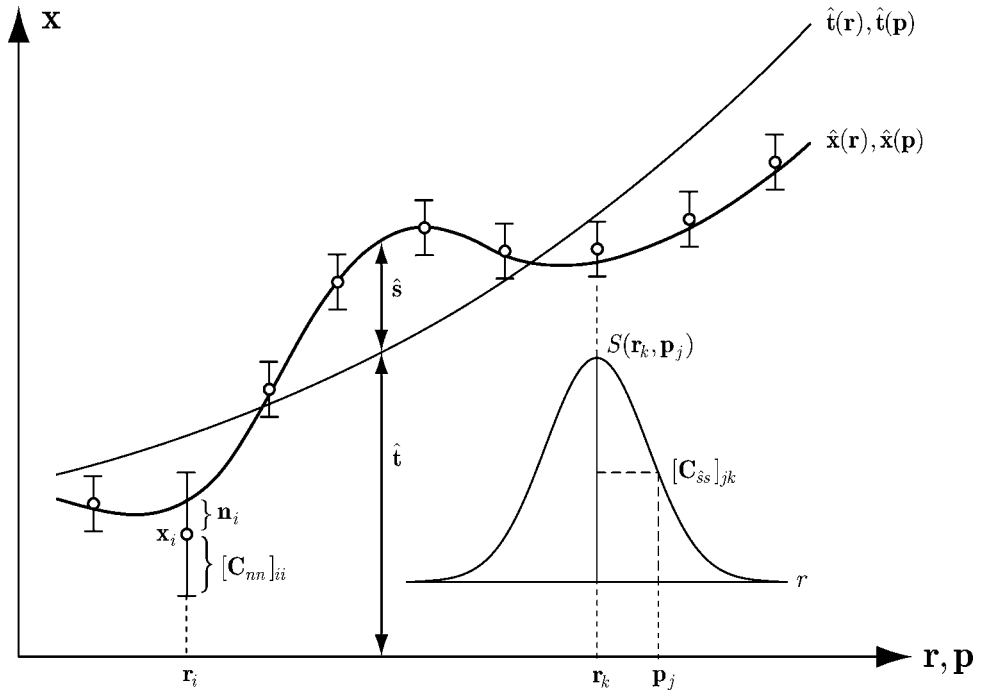

Figure 1. Interpolation of measurements (circles) with LSC.

of $s(\mathbf{r})$ depends by definition only upon the distance $r_{AB} = |\mathbf{r}_A - \mathbf{r}_B|$ between two points. With eqs (2)–(4) we introduce following estimates of $t(\mathbf{r})$ and $s(\mathbf{r})$:

$$\hat{\mathbf{t}} = \mathbf{C}_{\hat{t}t}(\mathbf{C}_{tt} + \mathbf{C}_{ss} + \mathbf{C}_{nn})^{-1}\mathbf{x}$$
$$\hat{\mathbf{s}} = \mathbf{C}_{\hat{s}s}(\mathbf{C}_{ss} + \mathbf{C}_{nn})^{-1}(\mathbf{x} - \hat{\mathbf{t}}), \quad (6)$$

$\mathbf{C}_{tt}$ and $\mathbf{C}_{\hat{t}t}$ are the inhomogeneous covariance matrices of $t(\mathbf{r})$, and $\mathbf{C}_{ss}$ is the homogeneous, isotropic covariance matrix of $s(\mathbf{r})$. Accordingly, the gradient of $t(\mathbf{r})$ is given by:

$$\nabla\hat{\mathbf{t}}_1 = (\nabla\mathbf{C}_{\hat{t}t})(\mathbf{C}_{tt} + \mathbf{C}_{ss} + \mathbf{C}_{nn})^{-1}\mathbf{x}. \quad (7)$$

Consider the limit case of a crust divided into K pseudo-rigid plates that move relative to each other. In this case, $\nabla t(\mathbf{r})$ is small within the plates and large along the boundaries. The resulting non-homogeneity of $t(\mathbf{r})$ shall be taken into account by following covariance function of $t(\mathbf{r})$:

$$T(\mathbf{r}_{ik}, \mathbf{r}_{jl}) = \sigma_t^2 f(\|\mathbf{r}_{ik} - \mathbf{r}_{jl}\| / r_t), \quad (8)$$

where $f(r) \geq 0$ is a positive, monotonically decreasing function of $r \geq 0$ with $f(0) = 1$, $\lim_{r\to\infty} f(r) = 0$, $-\infty < f'(r) < 0$, $f'(0) = 0$, and σ_t^2 is the variance of $t(\mathbf{r})$. Furthermore, $\mathbf{r}_{ik}$ is the kth measurement point within the ith block, $r_t > 0$ is a scaling factor, called correlation length, and $\|.\|$ is the norm in a metric defined by:

$$\|\mathbf{r}_{ik} - \mathbf{r}_{jl}\| = (1 - \rho\delta_{ij})\ |\mathbf{r}_{ik} - \mathbf{r}_{jl}|, \quad (9)$$

where $\delta_{ij} = 1$ if $i = j$ and $\delta_{ij} = 0$ else, and $0 \leq \rho < 1$ is a rigidity parameter. The model (8) has two limit cases, depending on the value of ρ. If $\rho = 0$ the correlation function is homogeneous and isotropic, a feature expected if there are no fault zones. On the other hand, if $\rho \to 1$, $\|\mathbf{r}_A - \mathbf{r}_B\|$ coincides with the geometric distance if the points A and B belong to the same block, and $\|\mathbf{r}_A - \mathbf{r}_B\| \to \infty$ if A and B belong to different blocks. Accordingly, $T(\mathbf{r}_{ik}, \mathbf{r}_{jl}) = \sigma_t^2$ if $i = j$ and $T(\mathbf{r}_{ik}, \mathbf{r}_{jl}) = 0$ else. The derivative of $T(\mathbf{r}_{ik}, \mathbf{r}_{jl})$ is zero for $i = j$, so that there is no strain within the plates. Thus, eq. (8) with $\rho \to 1$ describes a model with totally rigid plates and shear zones of thickness $r_t(1 - \rho) \to 0$, where the velocity of the ith plate is a weighted mean of the measured velocities of all points within that plate. Intermediate solutions with semi-rigid plates and shear zones on non-zero thickness are obtained using $0 < \rho < 1$ (Fig. 2). This example shows how the covariance function of an inhomogeneous field $t(\mathbf{r})$ is related to its gradient $\nabla t(\mathbf{r})$. The inhomogeneity of $t(\mathbf{r})$ can be taken into account by 'uncoupling' regions of the crust that are separated by a high gradient zone, mimicking the mechanical uncoupling across a fault. The mathematic counterpart of the 'uncoupling' of two regions is a change in the metric of the plane, as obtained with eq. (9). In the following we present a generalization of eq. (9) that is suitable for any inhomogeneous field $t(\mathbf{r})$.

A first estimate of the crustal strain is obtained with LSC and some starting assumptions about $T(\mathbf{r}_A, \mathbf{r}_B)$. Highly strained regions are characterized by large values of $|\nabla t(\mathbf{r})|$. Hence, $\nabla t(\mathbf{r})$ is used to define an appropriate coordinate transformation that increases the distance between points where the strain rate is high. This coordinate transformation defines a new metric that is used to calculate a better model for $T(\mathbf{r}_A, \mathbf{r}_B)$ using eq. (8). The new $T(\mathbf{r}_A, \mathbf{r}_B)$ allows a second estimate of the strain field, and so on. The result is an iterative procedure whose details are specified better in the following.

A first estimate $t^{(1)}(\mathbf{r})$ of $t(\mathbf{r})$ is calculated using eq. (6) and the correlation functions:

$$T^{(1)}(\mathbf{r}_i, \mathbf{r}_j) = \sigma_t^{2(1)} f\left(|\mathbf{r}_i - \mathbf{r}_j| / r_t^{(1)}\right)$$
$$S^{(1)}(\mathbf{r}_i, \mathbf{r}_j) = \sigma_s^{2(1)} f\left(|\mathbf{r}_i - \mathbf{r}_j| / r_s^{(1)}\right), \quad (10)$$

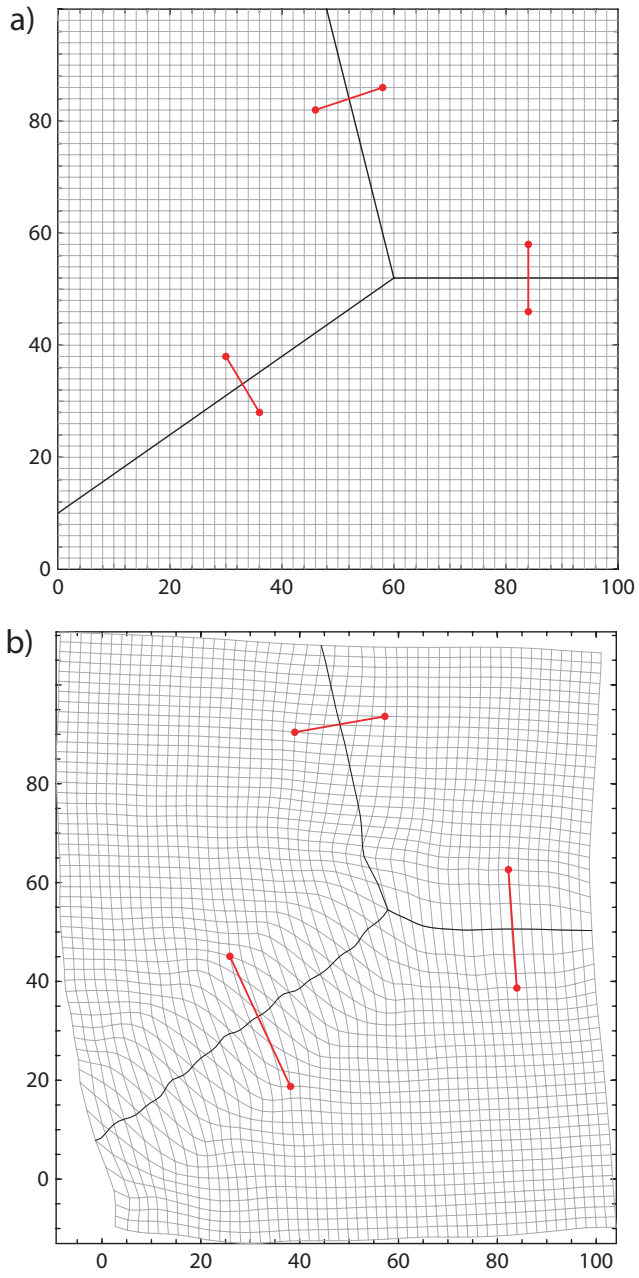

Figure 2. Example of coordinate transformation whose metric mimic the mechanical coupling between three plates (regions separated by thick black lines). The distance between two points that belong to different plates (red) is changed by an amount that depends on the strength of the faults (thick black lines). Large strain rate values occur at the shear zones, where the original Cartesian grid (grey lines) is stretched.

with initial guesses $r_t^{(1)}, r_s^{(1)}, \sigma_t^{2(1)}, \sigma_s^{2(1)}$ of $r_t, r_s, \sigma_t^2, \sigma_s^2$. The gradient $\nabla t^{(1)}(\mathbf{r})$ of $t^{(1)}(\mathbf{r})$ is calculated with eq. (7). New coordinates $\mathbf{r}_i^{(1)}$, $\mathbf{p}_i^{(1)}$ for the measurement and the prediction points are obtained using a coordinate transformation whose gradient matrix is linked to $\nabla t^{(1)}(\mathbf{r})$ as explained in the next section. These new coordinates are used to calculate new covariance matrices $\mathbf{C}_{tt}^{(2)}$, $\mathbf{C}_{\hat{t}t}^{(2)}$ with eq. (10). A second estimate $t^{(2)}(\mathbf{r})$ is obtained by inserting $\mathbf{C}_{tt}^{(2)}$, $\mathbf{C}_{\hat{t}t}^{(2)}$ in eq. (6). Again, $\nabla t^{(2)}(\mathbf{r})$ is used to define a new coordinate transformation and new covariance matrices, which in turn are used for the successive

estimate $t^{(3)}(\mathbf{r})$, and so on. The kth iteration is given by:

$$T^{(k)}(\mathbf{r}_i, \mathbf{r}_j) = \sigma_t^2 f\left(\left|\mathbf{r}_i^{(k-1)} - \mathbf{r}_j^{(k-1)}\right| / r_t^{(k)}\right)$$
$$S^{(k)}(\mathbf{r}_i, \mathbf{r}_j) = \sigma_s^2 f\left(\left|\mathbf{r}_i - \mathbf{r}_j\right| / r_s^{(k)}\right)$$
$$\hat{\mathbf{t}}^{(k)} = \mathbf{C}_{\hat{t}t}^{(k)}\left[\mathbf{C}_{tt}^{(k)} + \mathbf{C}_{ss}^{(k)} + \mathbf{C}_{nn}\right]^{-1}\mathbf{x}. \quad (11)$$

We call this iterative procedure *adaptative LSC*, ALSC, because the covariance matrix of the interpolation function is adapted to the specific properties of the interpolated field. A suitable coordinate transformation for ALSC is proposed in Section 3.

3 CONSTRUCTION OF A COORDINATE TRANSFORMATION FOR AN INHOMOGENEOUS METRIC

A suitable metric for eq. (8) may be easily defined by calculating the distance between two points with a weighted integral along a path that connects the points. The weighting function should depend on $\nabla t(\mathbf{r})$ along the integration path. However, the use of path integrals is computationally expensive, and the calculation of a $N \times M$ covariance matrix requires $\sim(NM)^2$ mathematical operations, instead of the $\sim NM$ operations required for a covariance matrix based on a Euclidian geometry. Thus, an alternative approach that requires only $\sim NM$ operations is presented in the following.

A suitable coordinate transformation can be constructed using a linear combination of elemental operators, each of which affects the metric of a small portion of the plane. We will call dilaton such an elemental operator, in analogy to an atom. A dilaton is a continuous and differentiable vector function $\mathbf{D}(\mathbf{r}, \mathbf{r}_0, \mathbf{u}_1, e_1, e_2, \gamma)$ in R^2 that defines a coordinate transformation:

$$\mathbf{r}' = \mathbf{r} + \mathbf{D}(\mathbf{r}, \mathbf{r}_0, \mathbf{u}_1, e_1, e_2, \gamma), \quad (12)$$

centred in $\mathbf{r}_0$, with an orientation given by the unit vector $\mathbf{u}_1$, scaling coefficients $e_1 > 0$, $e_2 > 0$, extension γ, and following properties:

$$\lim_{|\mathbf{r}-\mathbf{r}_0|/\gamma \to 0} \mathbf{r}' - \mathbf{r}_0 = e_1(\mathbf{r} - \mathbf{r}_0)\,\mathbf{u}_1 + e_2(\mathbf{r} - \mathbf{r}_0)\,\mathbf{u}_2, \quad (13a)$$

$$\lim_{|\mathbf{r}-\mathbf{r}_0|/\gamma \to \infty} \mathbf{r}' - \mathbf{r}_0 = 0, \quad (13b)$$

where $\mathbf{u}_1\mathbf{u}_2 = 0$ and $|\mathbf{u}_2| = 1$. According to (13a), a small region of radius $<\gamma$ around $\mathbf{r}_0$ is stretched along $\mathbf{u}_1$ and $\mathbf{u}_2$ by the factors e_1 and e_2, respectively. According to eq. (13b), the transformation does not affect the coordinates of points whose distance from $\mathbf{r}_0$ is $\gg\gamma$.

A simple analytical formulation of the dilaton that satisfies eqs 13(a) and (b) is:

$$\mathbf{D}(\mathbf{r}, \mathbf{r}_0, \mathbf{u}_1, e_1, e_2, \gamma) = \Delta(|\,\mathbf{r} - \mathbf{r}_0\,|, \gamma) \sum_{l=1}^{2} e_l(\mathbf{r} - \mathbf{r}_0)\,\mathbf{u}_l$$
$$\Delta(r, \gamma) = \frac{\gamma}{r}\tanh\left(\frac{r}{\gamma}\right), \quad (14)$$

with $l = 1, 2$. A geometric property of eq. (14) is that a set of circles with radii R, centred in $\mathbf{r}_0$, is transformed into a set of ellipses, centred in $\mathbf{r}_0$ and with half axes $\mathbf{a}\|\mathbf{u}_1$ and $\mathbf{b}\|\mathbf{u}_2$, with $|\mathbf{a}| = R + \gamma e_1 \tanh(R/\gamma)$ and $|\mathbf{b}| = R + \gamma e_2 \tanh(R/\gamma)$. Examples of coordinate transformations obtained using eqs (12) and (14) are shown in Fig. 3.

The gradient of the coordinate transformation is given by the directional derivative of $\mathbf{D}$ along a direction defined by a vector $\mathbf{n}$:

$$\frac{\partial}{\partial \mathbf{n}}\mathbf{D}(\mathbf{r}, \mathbf{r}_0, \mathbf{e}_1, \mathbf{e}_2, \gamma) = \sum_{l=1}^{2} e_l[\mathbf{G}(\mathbf{r} - \mathbf{r}_0, \mathbf{n}, \gamma)\,\mathbf{u}_l]\,\mathbf{u}_l$$
$$\mathbf{G}(\mathbf{r}, \mathbf{n}, \gamma) = (\mathbf{r}\,\mathbf{n})\frac{\mathbf{r}}{r^2}\sec h^2\frac{r}{\gamma} + \frac{\gamma}{r}\left[\mathbf{n} - (\mathbf{r}\,\mathbf{n})\frac{\mathbf{r}}{r^2}\right]\tanh\frac{r}{\gamma}. \quad (15)$$

Let us now consider a coordinate transformation obtained by the superposition of N dilaton functions with centres $\mathbf{r}_1, \ldots, \mathbf{r}_N$, and parameters $\mathbf{u}_1, \ldots, \mathbf{u}_N, e_{11}, \ldots, e_{N1}, e_{12}, \ldots, e_{N2}$:

$$\mathbf{r}' = \mathbf{r} + \sum_{k=1}^{N} \mathbf{D}(\mathbf{r}, \mathbf{r}_k, \mathbf{u}_k, e_{k1}, e_{k2}, \gamma). \quad (16)$$

According to eq. (15), the derivatives of eq. (15) at the point $\mathbf{r}_j$, $1 \le j \le N$, along two perpendicular directions defined by the unit vectors $\mathbf{d}_{j1}$, $\mathbf{d}_{j2}$ are given by:

$$\begin{cases} \sum_{k=1}^{N}\left[e_{k1}(\mathbf{G}_{kj1}\mathbf{u}_{k1})\,\mathbf{u}_{k1} + e_{k2}(\mathbf{G}_{kj1}\mathbf{u}_{k2})\,\mathbf{u}_{k2}\right] = d_{j1}\mathbf{d}_{j1} \\ \sum_{k=1}^{N}\left[e_{k1}(\mathbf{G}_{kj2}\mathbf{u}_{k1})\,\mathbf{u}_{k1} + e_{k2}(\mathbf{G}_{kj2}\,\mathbf{u}_{k2})\,\mathbf{u}_{k2}\right] = d_{j2}\mathbf{d}_{j2} \end{cases}, \quad (17)$$

with $\mathbf{G}_{kjl} = \mathbf{G}(\mathbf{r}_j - \mathbf{r}_k, \mathbf{d}_{jl}, \gamma)$, $|\mathbf{d}_{j1}| = 1$, $|\mathbf{d}_{j2}| = 1$ and $\mathbf{d}_{j1}\mathbf{d}_{j2} = 0$. If d_{j1}, d_{j2} and $\mathbf{d}_{j1}$ are given for all $1 \le j \le N$, eq. (17) is an overdetermined set of $4N$ non-linear equations with $2N$ unknowns e_{kl}, 1

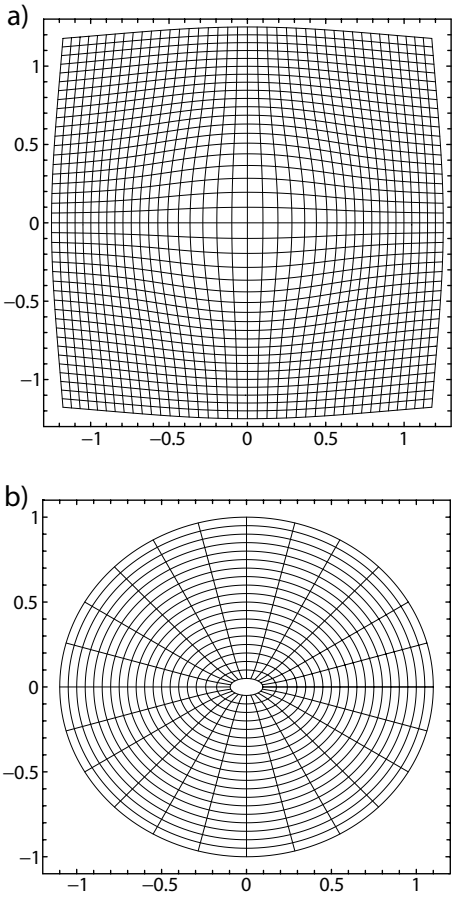

Figure 3. Examples of coordinate transformations with the dilaton operator defined by eq. (15). (a) Cartesian representation of $\mathbf{D}(\mathbf{r}, \mathbf{r}_0, \mathbf{u}_1, e_1, e_2, \gamma)$ with $\mathbf{r}_0 = 0$, $\mathbf{u}_1 = (1, 0)$, $e_1 = e_2 = 2$ and $\gamma = 0.25$. (b) Polar representation of $\mathbf{D}(\mathbf{r}, \mathbf{r}_0, \mathbf{u}_1, e_1, e_2, \gamma)$ with $\mathbf{r}_0 = 0$, $\mathbf{u}_1 = (1, 0)$, $e_1 = 3$, $e_2 = 1$ and $\gamma = 0.25$.

$\leq k \leq N$, $l = 1, 2$, and N unknowns for the orientations of $\mathbf{u}_{k1}$, $1 \leq k \leq N$. Thus, eq. (17) does not generally have a solution. However, if (1) $\nabla z(\mathbf{r}_j) = d_{j1}\mathbf{d}_{j1} + d_{j2}\mathbf{d}_{j2}$ is the gradient of a continuous and smooth function $z(\mathbf{r})$ at the point $\mathbf{r}_j$, (2) $\nabla z(\mathbf{r} + \gamma\mathbf{u}) \approx \nabla z(\mathbf{r})$ for any unit vector $\mathbf{u}$ and (3) the minimum distance between any couple of points $(\mathbf{r}_i, \mathbf{r}_j)$ is $\leq\gamma$, then the $\mathbf{r}_j$ are dense enough to assume $\mathbf{u}_{kl} \approx \mathbf{d}_{kl}$, $1 \leq k \leq N, l = 1, 2$. In this case, eq. (17) can be linearized to:

$$\begin{cases} \sum_{k=1}^{N} [e_{k1}(\mathbf{G}_{kj1}\mathbf{d}_{k1})\,\mathbf{d}_{k1} + e_{k2}(\mathbf{G}_{kj1}\mathbf{d}_{k2})\,\mathbf{d}_{k2}] = d_{j1}\mathbf{d}_{j1} \\ \sum_{k=1}^{N} [e_{k1}(\mathbf{G}_{kj2}\mathbf{d}_{k1})\,\mathbf{d}_{k1} + e_{k2}(\mathbf{G}_{kj2}\,\mathbf{d}_{k2})\,\mathbf{d}_{k2}] = d_{j2}\mathbf{d}_{j2} \end{cases} \tag{18}$$

which is still overdetermined. A scalar product of all equations in (18) with $\mathbf{d}_{j1}$, $\mathbf{d}_{j2}$ gives:

$$\begin{cases} \sum_{k=1}^{N} [e_{k1}(\mathbf{G}_{kj1}\mathbf{d}_{k1})\,(\mathbf{d}_{k1}\mathbf{d}_{j1}) + e_{k2}(\mathbf{G}_{kj1}\mathbf{d}_{k2})\,(\mathbf{d}_{k2}\mathbf{d}_{j1})] = d_{j1} \\ \sum_{k=1}^{N} [e_{k1}(\mathbf{G}_{kj1}\mathbf{d}_{k1})\,(\mathbf{d}_{k1}\mathbf{d}_{j2}) + e_{k2}(\mathbf{G}_{kj1}\mathbf{d}_{k2})\,(\mathbf{d}_{k2}\mathbf{d}_{j2})] = 0 \\ \sum_{k=1}^{N} [e_{k1}(\mathbf{G}_{kj2}\mathbf{d}_{k1})\,(\mathbf{d}_{k1}\mathbf{d}_{j1}) + e_{k2}(\mathbf{G}_{kj2}\,\mathbf{d}_{k2})\,(\mathbf{d}_{k2}\mathbf{d}_{j1})] = 0 \\ \sum_{k=1}^{N} [e_{k1}(\mathbf{G}_{kj2}\mathbf{d}_{k1})\,(\mathbf{d}_{k1}\mathbf{d}_{j2}) + e_{k2}(\mathbf{G}_{kj2}\,\mathbf{d}_{k2})\,(\mathbf{d}_{k2}\mathbf{d}_{j2})] = d_{j2} \end{cases} \tag{19}$$

For any two near points $\mathbf{r}_j$, $\mathbf{r}_k$ with $|\mathbf{r}_j - \mathbf{r}_k| \leq \gamma$, we can assume $\mathbf{d}_{k1}\mathbf{d}_{j2} \approx 0$, $\mathbf{d}_{k2}\mathbf{d}_{j1} \approx 0$ and $\mathbf{G}_{kj1}\mathbf{d}_{k2} \approx 0$, $\mathbf{G}_{kj2}\mathbf{d}_{k1} \approx 0$. On the other hand, for any two far points $\mathbf{r}_j, \mathbf{r}_k$ with $|\mathbf{r}_j - \mathbf{r}_k| \gg \gamma$, $\mathbf{G}_{kjl} \approx 0$. With these considerations, all the coefficients of the 2^{nd} and 3^{rd} equations of (19) are negligible, and we obtain:

$$\begin{cases} \sum_{k=1}^{N} [e_{k1}(\mathbf{G}_{kj1}\mathbf{d}_{k1})\,(\mathbf{d}_{k1}\mathbf{d}_{j1}) + e_{k2}(\mathbf{G}_{kj1}\mathbf{d}_{k2})\,(\mathbf{d}_{k2}\mathbf{d}_{j1})] = d_{j1} \\ \sum_{k=1}^{N} [e_{k1}(\mathbf{G}_{kj2}\mathbf{d}_{k1})\,(\mathbf{d}_{k1}\mathbf{d}_{j2}) + e_{k2}(\mathbf{G}_{kj2}\,\mathbf{d}_{k2})\,(\mathbf{d}_{k2}\mathbf{d}_{j2})] = d_{j2} \end{cases} \tag{20}$$

which is now a set of $2N$ linear equations in the $2N$ unknowns e_{kl}, $1 \leq k \leq N, l = 1, 2$. The solution of eq. (20) is:

$$\begin{bmatrix} \mathbf{e}_1 \\ \mathbf{e}_2 \end{bmatrix} = \begin{bmatrix} \mathbf{M}_{11} & \mathbf{M}_{12} \\ \mathbf{M}_{21} & \mathbf{M}_{22} \end{bmatrix}^{-1} \begin{bmatrix} \mathbf{v}_1 \\ \mathbf{v}_2 \end{bmatrix}, \tag{21}$$

with $[\mathbf{M}_{lm}]_{kj} = (\mathbf{G}_{kjl}\mathbf{d}_{km})(\mathbf{d}_{km}\mathbf{d}_{jl})$, $[\mathbf{e}_l]_k = e_{kl}$, $[\mathbf{v}_l]_j = d_{jl}$. Using eqs (14), (16) and (21) it is possible to find a coordinate transformation that produces a smooth deformation of the plane, whose gradient is specified on a sufficiently dense set of N points $\mathbf{r}_1, \ldots, \mathbf{r}_N$.

4 LINK BETWEEN COORDINATE TRANSFORMATION AND GRADIENT fiELD

Let d_1, d_2 be the eigenvalues of the gradient matrix $\nabla\mathbf{D}$ of a coordinate transformation $\mathbf{r} \mapsto \mathbf{r}' = \mathbf{r} + \mathbf{D}(\mathbf{r})$, with eigenvectors $\mathbf{d}_1$, $\mathbf{d}_2$. A reasonable criterion for choosing a suitable transformation is that $\mathbf{d}_1$ and $\mathbf{d}_2$ should coincide with the directions of the minimum and the maximum of the absolute value of the directional derivative $|\mathbf{u}\nabla\hat{t}|$, and that d_1, d_2 should be proportional to $g_1 = |\mathbf{d}_1\nabla\hat{t}|$ and $g_2 = |\mathbf{d}_2\nabla\hat{t}|$, respectively. In this way, the plane is stretched along the direction of maximal absolute gradient to an amount which is proportional to the gradient itself. The proportionality factor depends on the maximum allowed ratio μ of the distance $|\mathbf{r}'_A - \mathbf{r}'_B|$ of any two points A, B in the transformed coordinate system to the distance $|\mathbf{r}_A - \mathbf{r}_B|$ of the same points in the untransformed coordinate system. Hence:

$$\begin{aligned} d_{jl} &= \mu g_{\max}^{-1} |\,\mathbf{d}_{jl}\nabla\hat{t}(\mathbf{r}_j)| \\ g_{\max} &= \max_{1\leq j\leq N} \max_{|\mathbf{u}_j|=1} |\,\mathbf{u}_j\nabla\hat{t}(\mathbf{r}_j)|. \end{aligned} \tag{22}$$

If the parameters $\mathbf{d}_{j1}$, $\mathbf{d}_{j2}$, d_{j1}, d_{j2} are substituted in eq. (21) a suitable coordinate transformation is obtained. A synthetic 1-D example of such coordinate transformation is given in Fig. 4. The result of ALSC for this example has been compared with results of various smoothing splines and low-pass filters (Fig. 5). ALSC performed better than the alternative interpolation methods tested, both in terms of stability with respect to the fitting parameters (e.g. knots and polynomial order in the case of splines), and in the capability of handling highly inhomogeneous fields.

5 OPTIMAL CHOICE OF THE ALSC PARAMETERS

LSC is controlled by two parameters: the signal variance σ^2 and the signal correlation length r_0, defined with $f(r_0) = f(0)/2$, where $f(r)$ is the covariance function. Both parameters can be determined empirically, being σ^2 the variance of the measurements and $r_0 \geq \bar{r}$, whereby $\bar{r}$ is the average distance between the measurement points. On the other hand, ALSC is controlled by the five parameters σ_t, σ_s, r_t, r_s, and $g_{\max}$. The choice of these parameters is not free: σ_t and σ_s should correspond to the *a posteriori* estimates of the trend function variance and the signal variance, r_t to the typical autocorrelation length of the trend function, and r_s should not be smaller than $\bar{r}$. Therefore, we propose following rule-of-thumb for the choice of the ALSC parameters:

$$\begin{aligned} &\sigma_t^{(1)} = \sigma\ ,\ \ \sigma_s^{(1)} = 0 \\ &r_t^{(1)} \approx r_s \approx \bar{r} \\ &\sigma_t^{(k+1)} = \sigma_x - \sigma_s^{(k)} \\ &g_{\max}^{(k)} \leq r_t^{(k)}/\bar{r}\ ,\ r_t^{\text{final}} \approx \hat{r}_t > \bar{r}. \end{aligned} \tag{23}$$

The condition $g_{\max}^{(k)} \leq r_t^{(k)}/\bar{r}$ ensures that r_t is not smaller than $\bar{r}$ in the transformed coordinate system. The final choice of r_t should correspond to the typical autocorrelation length $\hat{r}_t$ of the estimated trend function.

The result of an ALSC interpolation, given by $\hat{t}(\mathbf{r}) + \hat{s}(\mathbf{r})$, depends weakly on the choice of trend function parameters discussed above, as long as $r_s \ll r_t$. The error of the ALSC interpolation is given by the error of the LSC interpolation of the short-range signal. On the other hand, a modified error estimation is required for $\hat{t}(\mathbf{r})$ and $\nabla\hat{t}(\mathbf{r})$, as discussed in the next section.

6 TREND GRADIENTS AND TREND ERROR ESTIMATION

The gradient calculation and the error estimation with LSC have been discussed in Moritz (1973). The calculation of a trend gradient with ALSC is very similar, but requires some additional steps due to the coordinate transformation. The same apply to the gradient error estimation. Following Moritz (1973), the error matrix $\mathbf{E}_{\hat{t}\hat{t}}$ of an interpolated (trend) field $\hat{t}$ is defined as $\mathbf{E}_{\hat{t}\hat{t}} = E(\varepsilon_t\varepsilon_t^{\mathrm{T}})$, where $\varepsilon_t = \hat{\mathbf{t}} - \tilde{\mathbf{t}}$ and $\tilde{\mathbf{t}}$ is the (unknown) error-free value of $\mathbf{t}$ on the

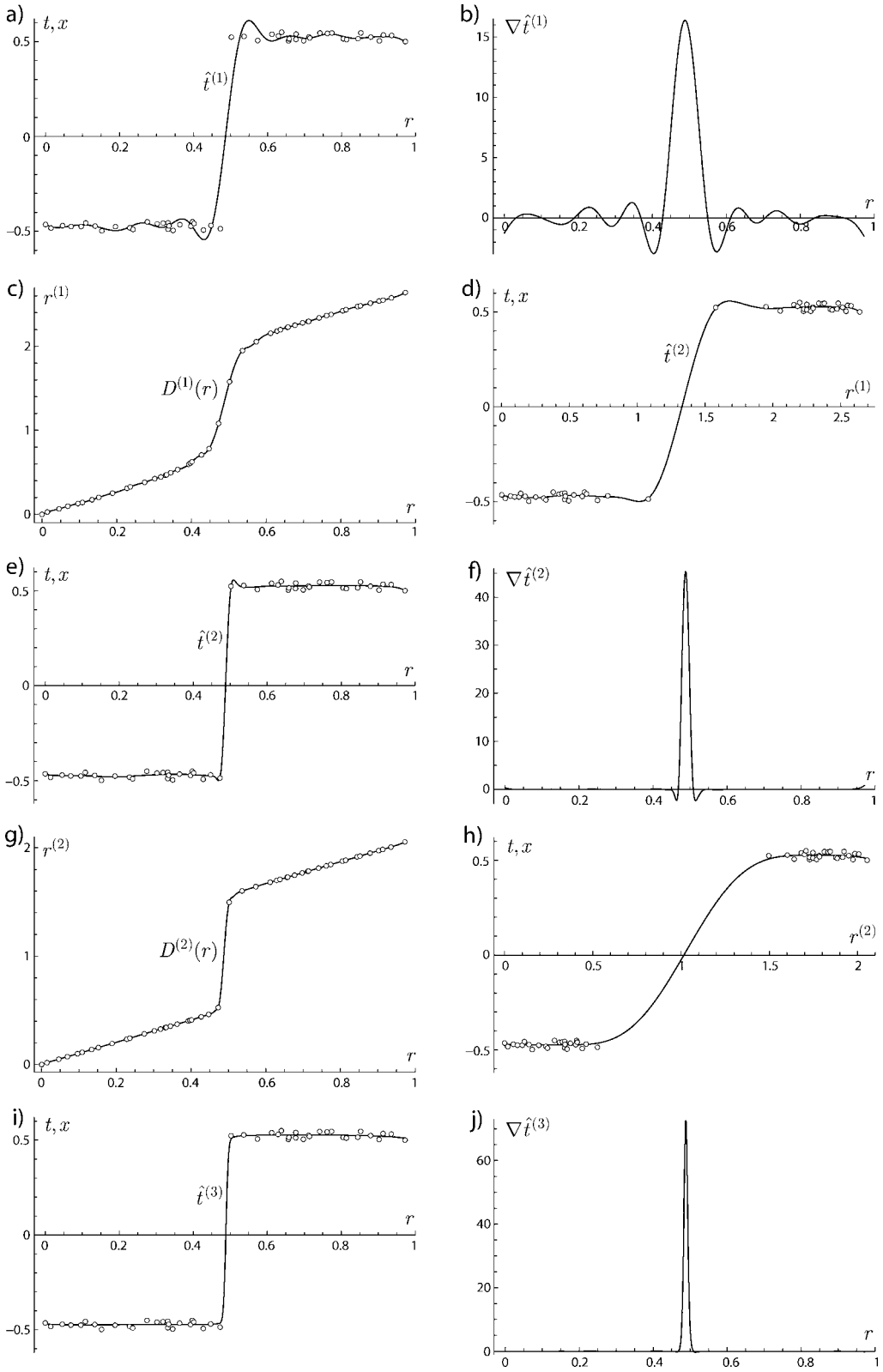

Figure 4. Synthetic 1-D example of block detection. The velocity field of two plates was simulated with a Heaviside unit step function evaluated at 50 measurement points (circles) affected by a Gaussian error with $\sigma = 0.05$. (a) First estimate $\hat{t}^{(1)}$ of the trend function and (b) its gradient $\nabla\hat{t}^{(1)}$, calculated with LSC and the covariance function $T^{(1)}(r) = \exp(-r^2/r_t^2)$, $r_t = 0.03$. (c) A coordinate transformation $r^{(1)} = D_1(r)$ increases the distance between the points by an amount which is proportional to $\nabla\hat{t}^{(1)}$. (d) A second estimate $\hat{t}^{(2)}$ of the trend function is calculated as in (a) with the covariance function $T^{(2)}(r) = T^{(1)}(r^{(1)})$, where $r^{(1)}$ is the distance between two points in transformed coordinates. (e) $\hat{t}^{(2)}$ in original coordinates and (f) the corresponding gradient. The procedure illustrated in (a–f) is repeated in (g–j) to obtain a third estimate $\hat{t}^{(3)}$ of the trend function that is very close to the Heaviside step function used to generate the synthetic measurements.

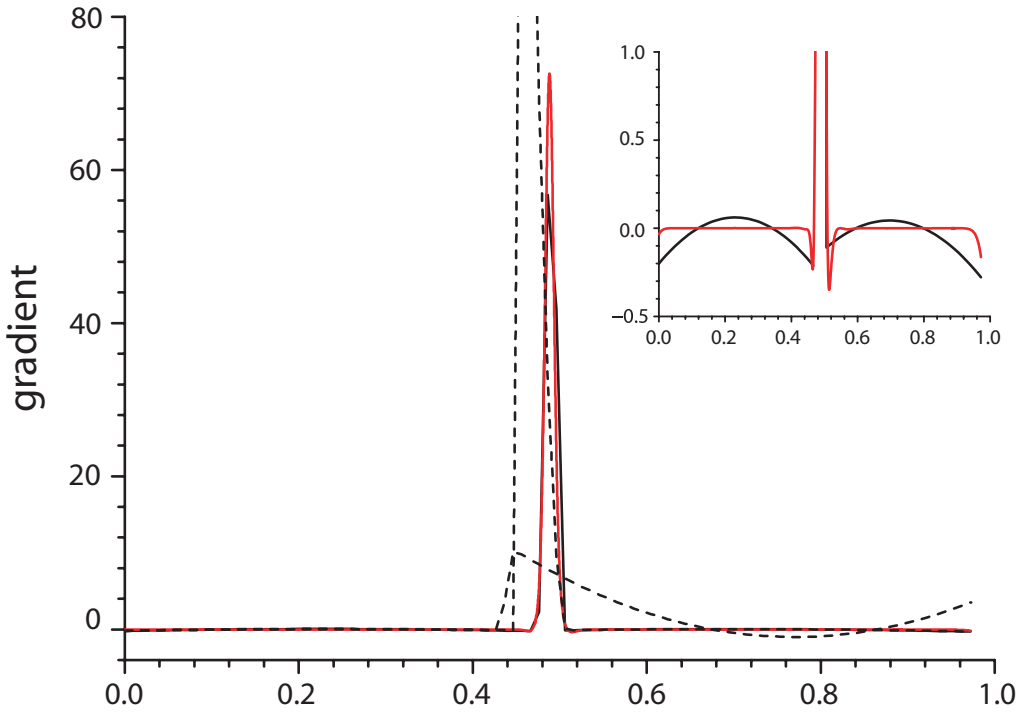

Figure 5. Comparison of gradient functions estimated using ALSC (solid curve, red) and the best result of different smoothing spline methods (solid curve, black), on the same data set of Fig. 4. Gradients are plotted on full scale and zoomed to show details far from the central peak (inset). The smoothing spline method shown is a least-squares optimized B-spline of third order with eight knot points. The result obtained with spline methods depends strongly on the parameters chosen. For example, adding or removing a knot point to the B-spline drives the interpolation into unstable solutions (dashed lines). Notice that the solution obtained with ALSC over the entire range is not affected by the central peak.

interpolation points. Thereafter:

$$\begin{aligned}\varepsilon_t \varepsilon_t^{\mathrm{T}} &= (\mathbf{H}\mathbf{x} - \tilde{\mathbf{t}})(\mathbf{H}\mathbf{x} - \tilde{\mathbf{t}})^{\mathrm{T}} \\ &= \mathbf{H}\mathbf{x}\,\mathbf{x}^{\mathrm{T}}\mathbf{H}^{\mathrm{T}} - \tilde{\mathbf{t}}\,\mathbf{x}^{\mathrm{T}}\mathbf{H}^{\mathrm{T}} - \mathbf{H}\,(\tilde{\mathbf{t}}\,\mathbf{x}^{\mathrm{T}})^{\mathrm{T}} + \tilde{\mathbf{t}}\,\tilde{\mathbf{t}}^{\mathrm{T}},\end{aligned} \tag{24}$$

where $\mathbf{H} = \mathbf{C}_{\hat{t}t}(\mathbf{C}_{tt} + \mathbf{C}_{ss} + \mathbf{C}_{nn})^{-1}$, and $\mathbf{x}$ is the measurements vector. If $\mathbf{t}$, $\mathbf{s}$ and $\mathbf{n}$ are independent, $E(\mathbf{x}\,\mathbf{x}^{\mathrm{T}}) = \mathbf{C}_{tt} + \mathbf{C}_{ss} + \mathbf{C}_{nn}$, $E(\tilde{\mathbf{t}}\,\tilde{\mathbf{t}}^{\mathrm{T}}) \cong \mathbf{C}_{\hat{t}\hat{t}}$, and $E(\tilde{\mathbf{t}}\,\mathbf{x}^{\mathrm{T}}) \cong \mathbf{C}_{\hat{t}t}$ and after some algebraic steps:

$$\mathbf{E}_{\hat{t}\hat{t}} = \mathbf{C}_{\hat{t}\hat{t}} - \mathbf{C}_{\hat{t}t}(\mathbf{C}_{tt} + \mathbf{C}_{ss} + \mathbf{C}_{nn})^{-1}\,\mathbf{C}_{\hat{t}t}^{\mathrm{T}}. \tag{25}$$

The gradient $\nabla\hat{t} = (\partial_x t, \partial_y t)$ of $\hat{t}$ is given by the derivatives along x and y, with:

$$\begin{aligned}\hat{t}_x &= \partial_x\hat{t} = \frac{\partial x'}{\partial x}\partial'_x\hat{t} + \frac{\partial y'}{\partial x}\partial'_y\hat{t} \\ \hat{t}_y &= \partial_y\hat{t} = \frac{\partial x'}{\partial y}\partial'_x\hat{t} + \frac{\partial y'}{\partial y}\partial'_y\hat{t},\end{aligned} \tag{26}$$

where (x', y') are the transformed coordinates according to Section 3. In vector form:

$$\begin{aligned}\hat{\mathbf{s}}_x &= \partial_x\hat{\mathbf{t}} = \mathbf{X}'_x\hat{\mathbf{t}}'_x + \mathbf{Y}'_x\hat{\mathbf{t}}'_y \\ \hat{\mathbf{s}}_y &= \partial_y\hat{\mathbf{t}} = \mathbf{X}'_y\hat{\mathbf{t}}'_x + \mathbf{Y}'_y\hat{\mathbf{t}}'_y,\end{aligned} \tag{27}$$

with $[\mathbf{X}']_{ij} = x'_i\delta_{ij}$, $[\mathbf{Y}']_{ij} = y'_i\delta_{ij}$. The explicit solution is:

$$\begin{aligned}\hat{\mathbf{t}}_x &= \left[\left(\mathbf{X}'_x\partial'_x + \mathbf{Y}'_x\partial'_y\right)\mathbf{C}_{\hat{t}t}\right](\mathbf{C}_{tt} + \mathbf{C}_{ss} + \mathbf{C}_{nn})^{-1}\mathbf{x} = \mathbf{G}_x\mathbf{x} \\ \hat{\mathbf{t}}_y &= \left[\left(\mathbf{X}'_y\partial'_x + \mathbf{Y}'_y\partial'_y\right)\mathbf{C}_{\hat{t}t}\right](\mathbf{C}_{tt} + \mathbf{C}_{ss} + \mathbf{C}_{nn})^{-1}\mathbf{x} = \mathbf{G}_y\mathbf{x}.\end{aligned} \tag{28}$$

The error matrix $\mathbf{E}_{t_x t_x}$ of $\hat{\mathbf{t}}_x$ is defined as $\mathbf{E}_{\hat{t}_x\hat{t}_x} = E(\varepsilon_{t_x}\varepsilon_{t_x}^{\mathrm{T}})$, where $\varepsilon_{t_x} = \hat{\mathbf{t}}_x - \tilde{\mathbf{t}}_x$. In analogy to eq. (24):

$$\begin{aligned}\varepsilon_{t_x}\varepsilon_{t_x}^{\mathrm{T}} &= \left(\mathbf{G}\mathbf{x} - \tilde{\mathbf{t}}_x\right)(\mathbf{G}\mathbf{x} - \tilde{\mathbf{t}}_x)^{\mathrm{T}} \\ &= \mathbf{G}\mathbf{x}\,\mathbf{x}^{\mathrm{T}}\mathbf{G}^{\mathrm{T}} - \tilde{\mathbf{t}}_x\,\mathbf{x}^{\mathrm{T}}\mathbf{G}^{\mathrm{T}} - \mathbf{G}\,(\tilde{\mathbf{t}}_x\,\mathbf{x}^{\mathrm{T}})^{\mathrm{T}} + \tilde{\mathbf{t}}_x\tilde{\mathbf{t}}_x^{\mathrm{T}}.\end{aligned} \tag{29}$$

With:

$$\begin{aligned}E\left(\tilde{\mathbf{t}}_x\mathbf{x}^{\mathrm{T}}\right) &\cong \left(\mathbf{X}'_x\partial'_x + \mathbf{Y}'_x\partial'_y\right)\mathbf{C}_{\hat{t}t} \\ E\left(\tilde{\mathbf{t}}_x\tilde{\mathbf{t}}_x^{\mathrm{T}}\right) &\cong \left(\mathbf{X}'_{xx}\partial'_x + \mathbf{Y}'_{xx}\partial'_y + \mathbf{X}'^2_x\partial_{x'x'} + \mathbf{Y}'^2_x\partial_{y'y'} + 2\,\mathbf{X}'_x\mathbf{Y}'_x\partial_{x'y'}\right)\mathbf{C}_{\hat{t}\hat{t}},\end{aligned} \tag{30}$$

and after some algebraic steps:

$$\begin{aligned}\mathbf{E}_{t_x t_x} = &\left(\mathbf{X}'_{xx}\partial'_x + \mathbf{Y}'_{xx}\partial'_y + \mathbf{X}'^2_x\partial_{x'x'} + \mathbf{Y}'^2_x\partial_{y'y'} + 2\,\mathbf{X}'_x\mathbf{Y}'_x\partial_{x'y'}\right)\mathbf{C}_{\hat{t}\hat{t}} \\ &- \left(\mathbf{X}'_x\partial'_x + \mathbf{Y}'_x\partial'_y\right)\mathbf{C}_{\hat{t}t}(\mathbf{C}_{tt} + \mathbf{C}_{ss} + \mathbf{C}_{nn})^{-1} \\ &\times\left[\left(\mathbf{X}'_x\partial'_x + \mathbf{Y}'_x\partial'_y\right)\mathbf{C}_{\hat{t}t}\right]^{\mathrm{T}}.\end{aligned} \tag{31}$$

A similar result is obtained for $\mathbf{E}_{t_y t_y}$ by exchanging x and y in eq. (31).

7 EXAMPLES

Two examples of ALSC are discussed in the following. The first example is based on synthetic data and shows how ALSC can handle extremely inhomogeneous fields. In the second example, ALSC is used in a real example to analyse precise levelling measurements over the Alps, where RCM's are complicated by the complex geological structure of the region.

7.1 A triple junction

In order to test the capability of ALSC to fit highly inhomogeneous fields, a synthetic data set was generated to simulate horizontal velocity measurements of a triple junction of infinitely rigid plates with the geometry of Fig. 2(a). Only one component of the velocity vector has been considered, assuming homogeneous measurements

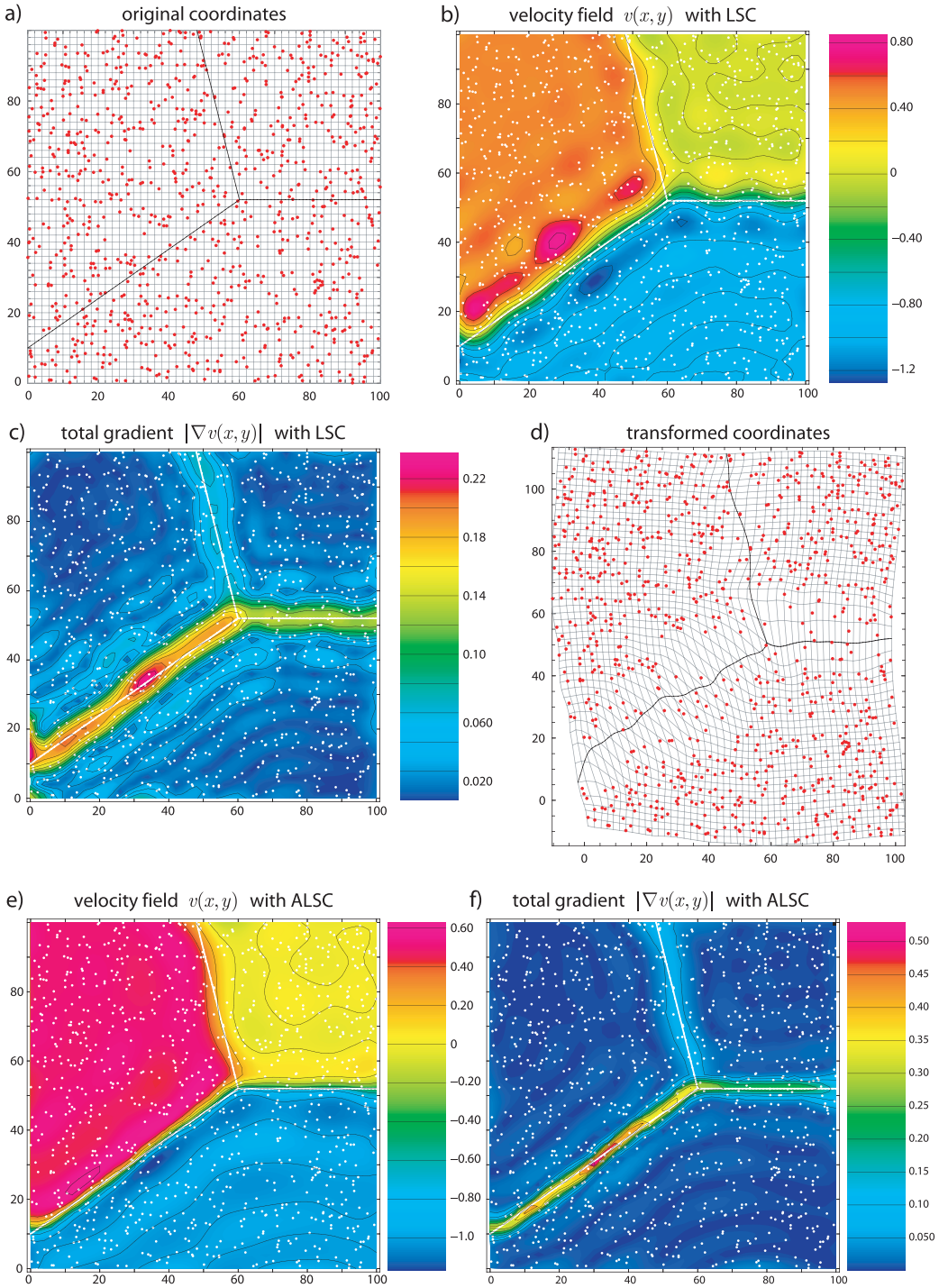

Figure 6. Synthetic 2-D example of block detection. 1000 simulated measurement points (white dots) are randomly distributed on three plates with velocities of −1, 0, and 0.5, respectively. (a) Original measurement coordinates (dots) and interpolation grid (grey). (b) LSC interpolation, and (c) total gradient of (a). (d) Transformed coordinates. (e) ALSC interpolation with the transformed coordinates of (d). (f) Total gradient of (e). See text for more details.

values of −1, 0, and 0.5 for the three plates (Fig. 6). The measurements have been simulated with 1000 points distributed randomly over a square area of 100 × 100. Thus, the mean distance between the measurements is $\bar{r} = 10$. Measurement errors have been simulated using a Gaussian random signal with a standard deviation 0.02. Accordingly, the error covariance matrix is given by $[\mathbf{C}_{nn}]_{ij} = 0.0004\,\delta_{ij}$. A first estimate of $t(\mathbf{r})$ was calculated using LSC and a covariance function given by $T(r) = \exp(-r^2/r_t^2)$, with $r_t = 12$ (Fig. 6b). The corresponding total gradient (Fig. 6c) has been used to define a coordinate transformation according to Sections 3 and 4 with $g_{\max} = 3$. The new coordinates define a new covariance function, which was in turn used to calculate a second estimate of $t(\mathbf{r})$. These steps have been repeated five times, while r_t was progressively increased to a final value of $r_t = g_{\max}\bar{r} = 30$. The final result is a function that follows closely the original velocity field (Figs 6e and f) and defines sharp shear zones along the plate boundaries. This

Table 2. Levelling lines in northern Italy. First column: measurement locations. Second column: estimated vertical velocities relative to a reference point in Genova (Arca & Beretta 1985). Third column: vertical velocities of the nearest points measured by the Swiss Federal Office of Topography, relative to a reference point in Aarburg. Fourth column: Differences between the second and third column.

Line	v, mm a^{-1} (Italy)	v, mm a^{-1} (Switzerland)	Δv
Quadrivio Ticino–Sempione			
Galleria del Sempione	+2.60	+1.05 ± 0.14 (Simplontunnel)	+1.55
Gravellona–Valmara			
Valmara	+2.30	+0.69 ± 0.18 (Brissago)	+1.61
Trivio–Chiavenna			
Chiavenna	+1.17	+1.05 ± 0.22 (Castasegna)	+0.50

result cannot be obtained with LSC: if the correlation length is small, the interpolation and its gradient affected by unrealistic oscillation induced by the sharp change of the measurement values at the plate boundaries. On the other hand, large values of the correlation length produce a smeared velocity field. The error standard deviation of the velocity field is 0.1 for the LSC interpolation (Fig. 6b), and 0.05 for the ALSC interpolation (Fig. 6e). The ratio of the maximal interpolated gradient within the three plates (expected to be 0), to the gradient at the plate junctions (expected to be ∞), is 0.25 for the LSC interpolation and 0.075 for the ALSC interpolation.

7.2 Interpolation of precise levelling measurements with ALSC

In the following, ALSC is applied to a real set of data. The data set of this example is a compilation of precise levelling measurements performed in Switzerland, Austria and Italy. These measurements cover a large portion of the Alps, and are a suitable database for an estimation of the vertical tectonic movements in the region. The main part of this data set, consisting in 1033 data points distributed over Switzerland has been kindly provided by the Swiss Federal Office of Topography (Swisstopo: www.swisstopo.ch). Swisstopo observes and maintains a levelling network with a length of about 3500 km with ≈10 000 control points. This so-called first- and second-order levelling network, initially measured between 1903 and 1945, is divided into 18 loops. From 1943 until the end of the 20th century almost all lines were measured a second time, and some of them even a third time. The average time interval between the observations reaches 50 yr. The differences between the first and the second (third) measurements, divided by the time interval, gives the average vertical velocities at the measuring points. Similar repeated measurements have been performed in Austria and Italy as well. First levelling measurements in northern Italy have been performed between 1877 and 1903 by the IGM (Istituto Geografico Militare), some of these measurements have been repeated between 1950 and 1956 (Arca & Beretta 1985). Data for the western part of Austria have been kindly provided by the BEV (Bundesamt für Eich- und Vermessungswesen). The data sets of Austria and Italy complete some open levelling loops in the S and E part of Switzerland. Swiss levelling measurements are relative to a reference point in Aarburg, where the vertical velocity has been set arbitrary to zero. The Italian levelling reference point is a mareograph situated at Genova, and the Austrian reference point is located at Horn. Because of the relative velocity of these reference points, there is a systematic offset between the three data sets. Fortunately, some common or very close points near the Swiss border have been measured by two countries. A comparison of these measurements gives the approximate offset between the different data sets (Table 2). The error covariance matrix must account for the error propagation along the levelling lines (Gubler *et al.* 1984). For the Swiss levelling, this error propagation is given by $\delta v \approx 0.015\, r^{1/2}$, where δv in mm a^{-1} is the error of the relative velocity of two points located at a distance r in km (Fig. 7). For the Italian levelling, the error propagation of the

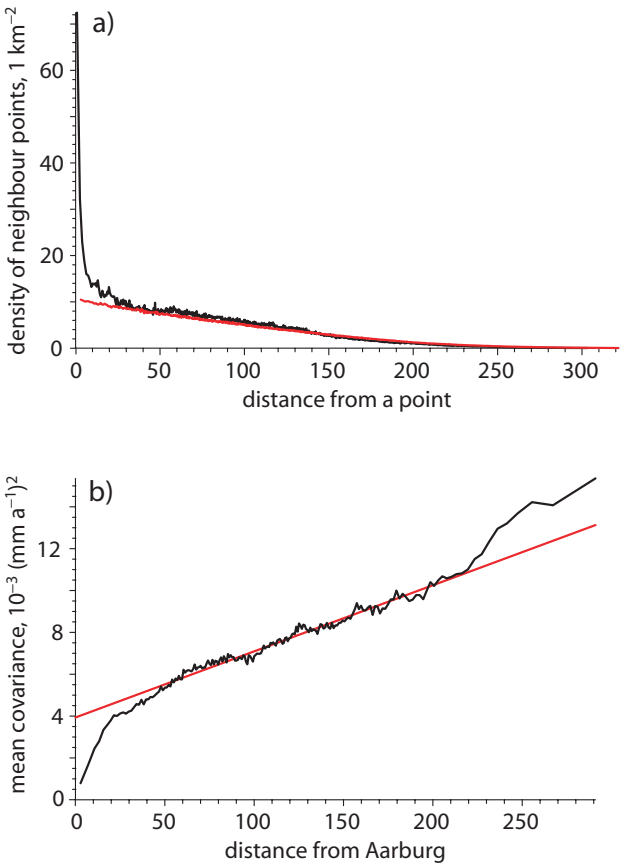

Figure 7. Statistical properties of 1033 precise levelling measurements in Switzerland. (a) Spatial distribution of the measuring points, expressed as the density of all measurements located at a given distance from each measuring point (black line). The distribution of 1033 random points within the country is shown for comparison (red line). The departure from a random distribution for distances <25 km is related to the mean diameter of the closed loops defined by levelling lines (see text). (b) Dependence of the error covariance matrix on the distance from the reference point in Aarburg (black line). The initial trend cov $(r) \approx 2.2 \times 10^{-4} r$ for distances $r < 25$ km reflects the measurement error propagation along individual the measuring lines. The red line marks the trend for $r > 25$ km, which characterizes the error propagation across closed measurement loops. The departure from this trend for $r > 220$ km is due to the presence of open loops in the southern part of Switzerland (Fig. 7).

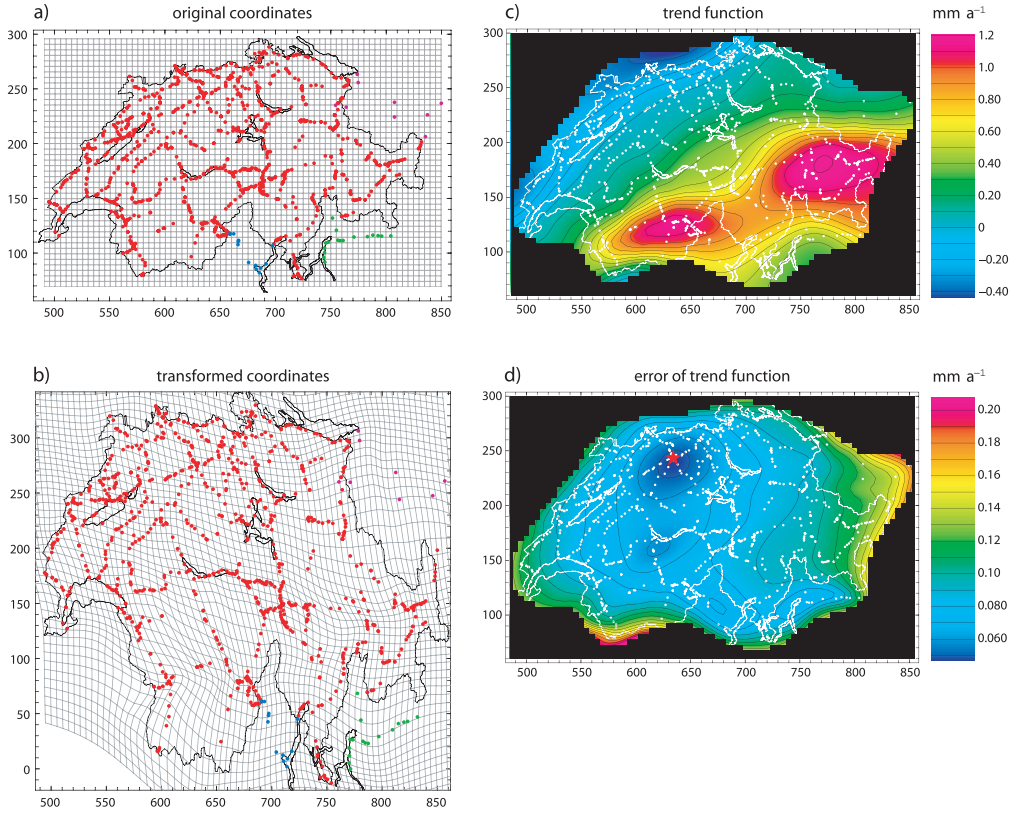

Figure 8. Trend function of vertical movements over the Alps calculated with ALSC from precise levelling measurements in Switzerland and neighbour countries. (a) Swiss coordinates of the measurements in km (dots), and interpolation grid (grey lines). Measurements have been performed by the Swiss Federal Office of Topography (red dots), the IGM (Istituto Geografico Militare, Italy, blue and green dots), and the BEV (Bundesamt für Eich- und Vermessungswesen, Austria, violet dots). (b) Transformed coordinates of the measurements. (c) Trend function calculated with ALSC and (d) corresponding error standard deviation. Notice the uplift rates of $\approx$1.2 mm a^{-1} over the Alps. As expected from the error covariance matrix (Fig. 7), the estimated error increases with increasing distances from the reference point in Aarburg (red star).

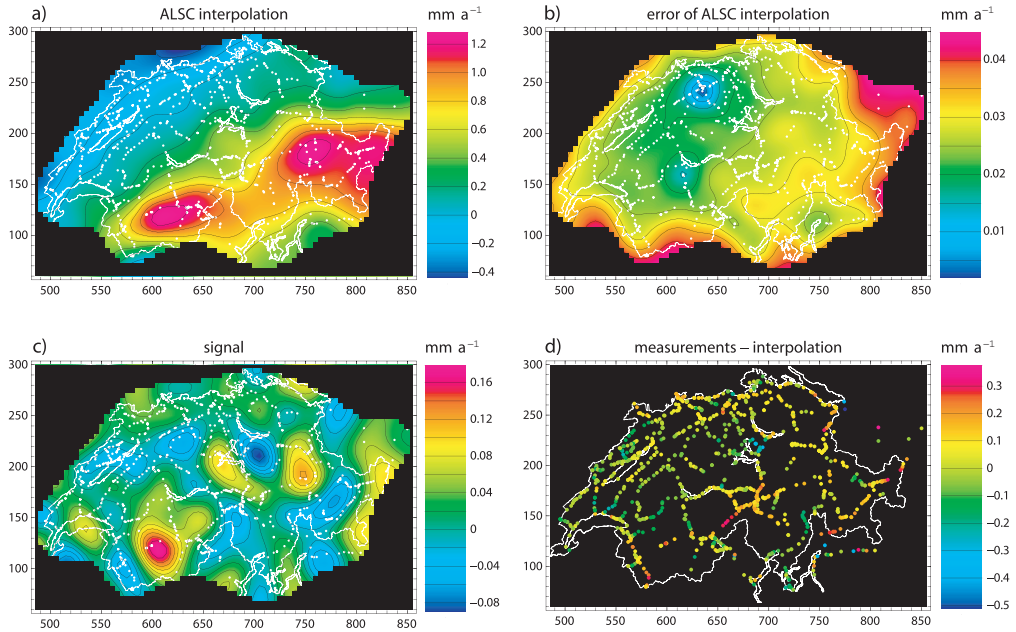

Figure 9. ALSC interpolation of precise levelling measurements in Switzerland and neighbour countries. (a) ALSC interpolation of the measurements and (b) estimated error standard deviation. (c) Stochastic component of the measurements (signal). The 'anomalies' in the central part, in the SW part and in the E part of Switzerland coincide with regions of enhanced seismic activity (see text). (d) Differences between measurements and ALSC interpolation. Anomalous levelling lines as well as some outliers can be recognized.

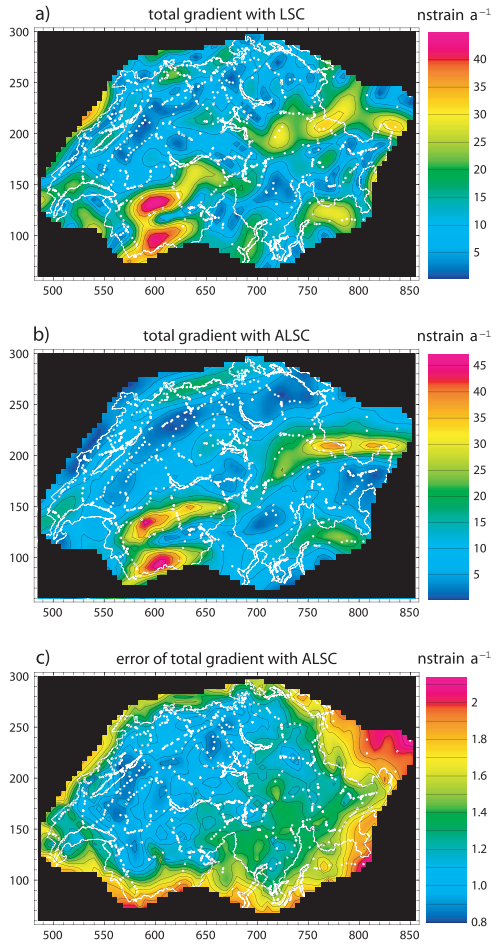

Figure 10. Comparison between the total gradient of vertical movements in Switzerland and neighbour countries, obtained (a) with LSC interpolation and (b) with ALSC interpolation. In (c) the error standard deviation of (b) is plotted. The gradient field obtained with ALSC shows more clearly the regions of high deformation along the Alpine arc and is more stable near the boundaries of the data set.

measurements is given by $\delta z \approx 1.13\, r^{1/2}$, where δz in mm is the error of the height difference of two points located at a distance r in km (Arca and Beretta 1985). Since the time interval between the first and the second levelling campaign is ≈50 yr, $\delta v \approx 0.023\, r^{1/2}$ for the Italian levelling lines. The elements of the error covariance matrix between the Swiss and the Italian measurements have been calculated as follows:

$$[\mathbf{C}_{nn}]_{\mathrm{CH}j,\mathrm{I}k} = [\mathbf{C}_{nn}]_{\mathrm{CHI,CH}j} + [\mathbf{C}_{nn}]_{\mathrm{CH}c,\mathrm{I}k}$$
$$[\mathbf{C}_{nn}]_{\mathrm{CH}c,\mathrm{I}k} = 5.1 \times 10^{-4} |\mathbf{r}_{\mathrm{CH}c} - \mathbf{r}_{\mathrm{I}k}|, \qquad (32)$$

where CHj is the jth point of the Swiss data set, I k is the kth point of an Italian levelling line and CHI is the common point between the two data sets (Table 2). A similar equation has been applied to the Austrian data. The levelling loops have a mean radius of 25 km. For distances >25 km the spatial distribution of measurements coincides with that of an equally large set of randomly distributed points (Fig. 8), and can be considered homogeneous. Hence, $\bar{r} = 25$ km is a reasonable estimate of the mean distance between the measurements. The measurements are expected to contain a contribution from a regional trend that reflects the uplift of the Alps (Gubler *et al.* 1981; Geiger *et al.* 1993), with superimposed local 'anomalies' related to specific geologic structures. In this case, the interpretation of the measurements as the superposition of a generic trend function $t(\mathbf{r})$ with non-isotropic, non-homogeneous covariance function, and a stochastic field $s(\mathbf{r})$ is physically justified.

A first estimate $\hat{t}^{(1)}$ of the trend function was obtained using LSC and the covariance function $T^{(1)}(r) = \sigma_t^2 \exp(-r^2/r_t^2)$, where $\sigma_t = 0.482$ mm a^{-1} is the standard deviation of the measurements and $r_t = \bar{r} = 25$ km is the correlation length. The trend function is dominated by the high uplift rates measured in the Alpine region, along a SWW–NEE oriented band with a lateral extension of ≈60 km.

An ALSC interpolation with 5 iterations has been performed, starting from $\hat{t}^{(1)}$, and choosing $r_t^{\mathrm{final}} = 60$ km, $S(r) = \sigma_s^2 \exp(-r^2/r_s^2)$ with $r_s = 30$ km and $\sigma_s^{(1)} = 0$, and $g_{\max} = r_t^{\mathrm{final}}/\bar{r} \approx 2.4$. The final results are plotted in Figs 8–10. A large part of the measured signal is accounted by $t(\mathbf{r})$, whereas $s(\mathbf{r})$ shows some significant excursions only

(i) between the Lakes of Zürich and Lucerne in the central part of Switzerland,
(ii) along the Rhône valley in the SW and
(iii) around Thusis in the E (Fig. 9).

Interestingly, these excursions coincide with some seismic active regions (labelled H3, H2-P1, P2 in Kastrup *et al.* 2004).

The advantages of the ALSC interpolation are particularly evident if the absolute gradient field of the vertical velocity is compared with the same result obtained with LSC and $r_0 = 30$ km (Fig. 10). Despite the same spatial 'resolution' determined by r_s and r_0, the ALSC interpolated gradient follows more clearly the Alpine arc and is not affected by the numerous 'oscillations' that occur in the LSC interpolation, especially at the boundaries of the data set and along the Alps.

8 CONCLUSIONS

ALSC is an optimized LSC method for the interpolation of non-stochastic fields, such as RCM. ALSC has been tested with synthetic data and with precise levelling measurements over the Alps. The synthetic tests demonstrated the superior ability of ALSC to interpolate extremely inhomogeneous fields, in comparison to LSC and smoothed splines methods. The better performance of ALSC is particularly evident in the calculation of gradient fields. ALSC results are stable against abrupt spatial variations of the interpolated field, and against truncation effects that may occur at the boundary of the region covered by the data. Ringing effects, expressed by the ratio of interpolated gradient amplitudes within zones of constant velocity to the maximum gradient, were reduced by 75 per cent using ALSC instead of LSC.

ALSC was tested on precise levelling measurements in the Alpine region, which represent a real example of highly inhomogenous and anistotropic velocity field. The ALSC interpolation clearly displayed a strong NNW–SSE gradient in the uplift velocity, concentrated in two narrow zones of 20 km thickness N, respectively south of the Alpine Arc. A LSC interpolation of the same data set was either too smooth, or it was dominated by ringing effects, depending on the correlation length chosen.

ACKNOWLEDGMENTS

We are grateful to N. Höggerl (Bundesamt für Eich- und Vermessungswesen) for providing us with precise levelling measurements of western Austria, and to M. Pierozzi (Istituto Geografico Militare) for information about the Italian levelling system. The manuscript

benefited from the constructive comments of two anonymous reviewers.

REFERENCES

Arca, S. & Beretta, G.P., 1985. Prima sintesi geodetico-geologica sui movimenti verticali del suolo nell'Italia Settentrionale, *Bollettino di Geodesia e Scienze Affini,* **44,** 125–156.

Chen, Q., Freymueller, J.T., Wang, Q., Yang, Z., Xu, C. & Liu, J., 2004. A deforming block model for the present-day tectonics of Tibet, *J. geophys. Res.,* **109,** doi:10.129/2002JB002151.

Cocard, M., Kahle, H.-G., Peer, Y., Geiger, A., Veis, G., Felekis, S., Paradissis, D. & Billiris, H., 1999. New constraints on the rapid crustal motion of the Aegean region: recent results inferred from GPS measurements (1993–1998) across the West Hellenic Arc, Greece, *Earth planet. Sci. Lett.,* **172,** 39–47.

Geiger, A., Kahle, H.-G., Straub, C., Müller, S., Bär, M. & Deichmann, N., 1993. Geodetic measurements and their impact on the modelling of recent crustal deformations in the Alpine region, *IAG Proceeding,* **112,** 369–372.

Grafarend, E.W., 1976. Geodetic applications of stochastic processes, *Phys. Earth planet. Inter.,* **12,** 151–179.

Gubler, E., Kahle, H.-G., Klingelé, E., Müller, S. & Olivier, R., 1981. Recent crustal movements in Switzerland and their interpretation, *Tectonophysics,* **71,** 125–152.

Gubler, E., Schneider, D. & Kellerhals, P., 1984. Bestimmung von rezenten Bewegungen der Erdkruste mit geodätischen Methoden, *NAGRA Technischer Bericht*.

Kahle, H.-G., Müller, M.V., Geiger, A., Danuser, G., Müller, S., Veis, G., Billiris, H. & Paradissis, D., 1995. The strain field in northwestern Greece and the Ionian Islands: results inferred from GPS measurements, *Tectonophysics,* **249,** 41–52.

Kahle, H.-G. *et al.*, 1999. The GPS strain field in the Aegean Sea and western Anatolia, *Geophys. Res. Lett.,* **26,** 2513–2516.

Kahle, H.-G., Cocard, M., Peter, Y., Geiger, A., Reilinger, R., Barka, A. & Veis, G., 2000. GPS-derived strain rate field within the boundary zones of the Eurasian, African, and Arabian plates, *J. geophys. Res.,* **105,** 23 353–23 370.

Kastrup, U., Zoback, M.L., Deichmann, N., Evans, K.F., Giardini, D. & Michael, A.J., 2004. Stress field variations in the Swiss Alps and the northern Alpine foreland derived from inversion of fault plane solutions, *J. geophys. Res.,* **109,** B01402 doi:10.1029/2003JB002550.

Kaula, W.M., 1963. Determination of the Earth's gravitational field, *Rev. Geophys.,* **1,** 507–551.

Krarup, T., 1969. A contribution to the mathematical foundation of physical geodesy, *Danish Geodetic Institute, Copenhagen,* **44**.

McKenzie, D. & Jackson, J., 1986. A block model of distributed deformation by faulting, *J. geol. Soc. Lond.,* **143,** 349–353.

McKlusky, S.C., Bjornstad, S.C., Hager, B.H., King, R.W., Meade, B.J., Miller, M.M., Monastero, F.C. & Souter, B.J., 2001. Present day kinematics of the eastern Californa shear zone from a geodetically constrained block model, *Geophys. Res. Lett.,* **28,** 3369–3372.

Moritz, H., 1970a. Least-squares estimation in physical geodesy, *Veröffentlichungen der Deutschen Geodätischen Kommission A,* **69**.

Moritz, H., 1970b. Combination of satellite harmonics and gravimetry, *Reports of the Dept. of Geodetic Science, Ohio State Univ.,* **146**.

Moritz, H., 1973. Least-Squares Collocation, *Deutsche Geodätische Kommission, Reihe A: Theoretische Geodäsie,* **75,** 1–91.

Moritz, H., 1978. Least-squares collocation, *Reviews of Geophysics and Space Physics,* **16,** 421–430.

Moritz, H., 1980. *Advanced Physical Geodesy,* Abacus Press, p. 500.

Morrison, F., 1977. Azimuth-dependent statistics for interpolating geodetic data, *Bullétin de Geodésie,* **51,** 105–118.

Rummel, R. & Schwarz, K.P., 1977. On the nonhomogeneity of the global covariance function, *Bullétin de Geodésie,* **51,** 93–103.

Sansò, F., 1980. The minimum mean square estimation error principle in physical Geodesy (stochastic and non-stochastic interpretation), *Bollettino di Geodesia e Scienze Affini,* **39,** 111–129.